Role of antioxidants in swift heavy ion tracks in polypropylene

Shankar Dutt [a],*, Pavel Apel [b], Olga Polezhaeva [b], Alexander Kiy [a], Nahid Afrin [a], Christian Notthoff [a], Nigel Kirby [c], Patrick Kluth [a]

[a] Department of Materials Physics, Research School of Physics, Australian National University, Canberra, ACT, 2601, Australia
[b] Flerov Laboratory of Nuclear Reactions, Joint Institute for Nuclear Research, 141980, Dubna, Moscow region, Russia
[c] ANSTO-Australian Synchrotron, Melbourne, Australia

A B S T R A C T

Using synchrotron-based small angle X-ray scattering, ion tracks created in polypropylene foils with different antioxidant contents were investigated. Tracks were created by irradiation with ^{197}Au, ^{209}Bi, and ^{132}Xe ions of energies 2.2 GeV, 710 MeV, and 160 MeV, respectively. The influence of antioxidant concentration in the polymer foils and aging of the samples on the structure of the ion tracks was explored. Polypropylene foils with high antioxidant content show a cylindrical track structure with a highly damaged core with significant mass loss and a gradual transition to the undamaged material. The size of the ion track can directly be correlated to the energy loss. On the other hand, ion tracks in low antioxidant content polypropylene foils exposed to Au/Bi ions reveal a cylindrical core shell structure with an over-dense shell area and a core region that is less dense than the pristine polymer. Oxygen uptake in the foils by the free radicals produced in the shell during the ion irradiation process was attributed to this structure due to prolonged exposure to ambient atmosphere. An overall mass increase was observed for these samples, consistent with the SAXS measurements and additional oxidation in a damaged halo produced by tracks.

1. Introduction

When swift heavy ions with energies ranging from tens of MeV to a few GeV traverse through organic and inorganic materials, they primarily interact with the target electrons, leading to ionization and electronic excitations. The coupling of this energy into the atomic system can result in the formation of 'ion tracks,' which are narrow, long damage trails. Often, ion track damage is significantly more susceptible to chemical etching than the undamaged material. This property can be used for the fabrication of nanopores with extremely narrow size distributions in a variety of materials. For decades, researchers have been interested in track-etched nanopore membrane fabrication in various polymers for applications such as nanowire fabrication, purification of protein solutions, isolation of exosomes, chemical and bio-sensing, gas separation, water desalination, virus detection, light and pH-responsive membranes, size-selective filtration and separation, and environmental studies [1–27]. More recently, channels with an even smaller (≤1 nm) effective radius have been formed without the need for chemical etching by illuminating the irradiated polymers with UV light and subsequent application of a transmembrane bias in an electrolyte. Such polymer membranes can be exploited for applications such as highly selective ion separation [28–30]. To thoroughly understand the process of track transformation into nanochannels as well as to leverage it for various applications, a comprehensive understanding of the track structure and

how it varies depending on the ion irradiation parameters and polymer composition is highly desired.

Polypropylene (PP) was invented in 1954 and soon gained popularity among researchers and industry due to its low density (~0.91 g/cm^3) compared to other common polymers including polyethylene, polycarbonate, polyethylene terephthalate, and polyamide [31]. It is presently the second-most extensively manufactured plastic due to interesting characteristics such as high chemical resistance, good hardness and fatigue resistance, and simplicity of machining [32]. Typically, isotactic polypropylene is used for the production of high quality semicrystalline biaxially oriented foils via the extrusion and stretching process [33]. With over 6 million tonnes per year, biaxially oriented PP foils have the biggest market share in terms of foil products [34]. Still, only few investigations have focused on the creation of nanopores in PP films [35–39], and little is known about the formation of ion tracks, including how it is affected by the ion energy, ion type, energy loss, and the particular structure of the polymer.

PP is particularly vulnerable to oxidation, and practically all commercial PP films contain antioxidants and stabilisers to avoid rapid breakdown under solar radiation and other conditions. The antioxidant content varies for different products, altering the polymer's oxidation-degradation characteristics. The oxidative stability of the PP film also dictates the degradation of the film's mechanical characteristics. Oxidation degradation of PP films has been well known for decades, and

---

* Corresponding author.
  E-mail address: shankar.dutt@anu.edu.au (S. Dutt).

many theories to explain the oxidation phenomena and chain-branching process have been proposed [31,32,40–45].

In the present study we are investigating the structure of ion tracks in PP films with different antioxygen contents and under a variety of irradiation conditions. We have used small angle X-ray scattering to investigate the structure and the radial density profile of the ion tracks. Although researchers have used microscopy techniques, most recently scanning electron microscopy (SEM), to observe ion tracks in semi-crystalline polymers by using controlled photo-oxidation and subsequent fracture [46], the details about the radial density distribution as well as small changes in the ion track structure are not easily accessible through microscopy techniques. SAXS is a non-destructive method based on the elastic scattering of monochromatic X-rays resulting from density fluctuations on a nanometre to micrometre scale and is a well-suited technique for determining the size and structure of ion tracks and nanometre-sized particles [47–50]. As it measures hundreds of thousands of ion tracks simultaneously, SAXS provides statically reliable and accurate information about the ion tracks. The results presented in this study not only add to the fundamental understanding of ion tracks in polypropylene but will also aid in the design of applications for ion tracks in polypropylene.

2. Experimental

2.1. Irradiation of PP foils

To investigate the influence of antioxidant content, ion type and electronic energy loss on the structure of ion tracks, two distinct types of polypropylene foils (Torayfan T2400 and Torayfan T2372, Toray, Japan) of density ~0.91 g/cm^3 with variable antioxidant content, each with a thickness of 10 μm, were irradiated at normal incidence with three different ions with different energies. Both the foils are semi-crystalline in nature and exhibit ~70% crystallinity. Polypropylene foil type T2372 has, according to supplier specifications, approximately five times the antioxidant content as compared to the foil type T2400. To qualitatively compare the differences in antioxidant content in these foils, an Evolution 600 spectrophotometer (Thermo Scientific) was used to measure UV spectra of unirradiated polypropylene foils. Fig. 1 shows the measured UV spectra for both foil types. The presence of hindered phenols in the foils is attributed to three peaks at ~198 nm, ~228 nm,

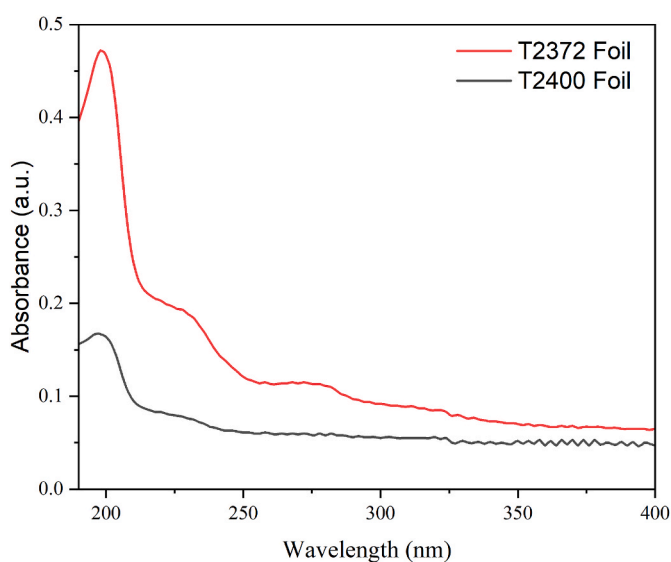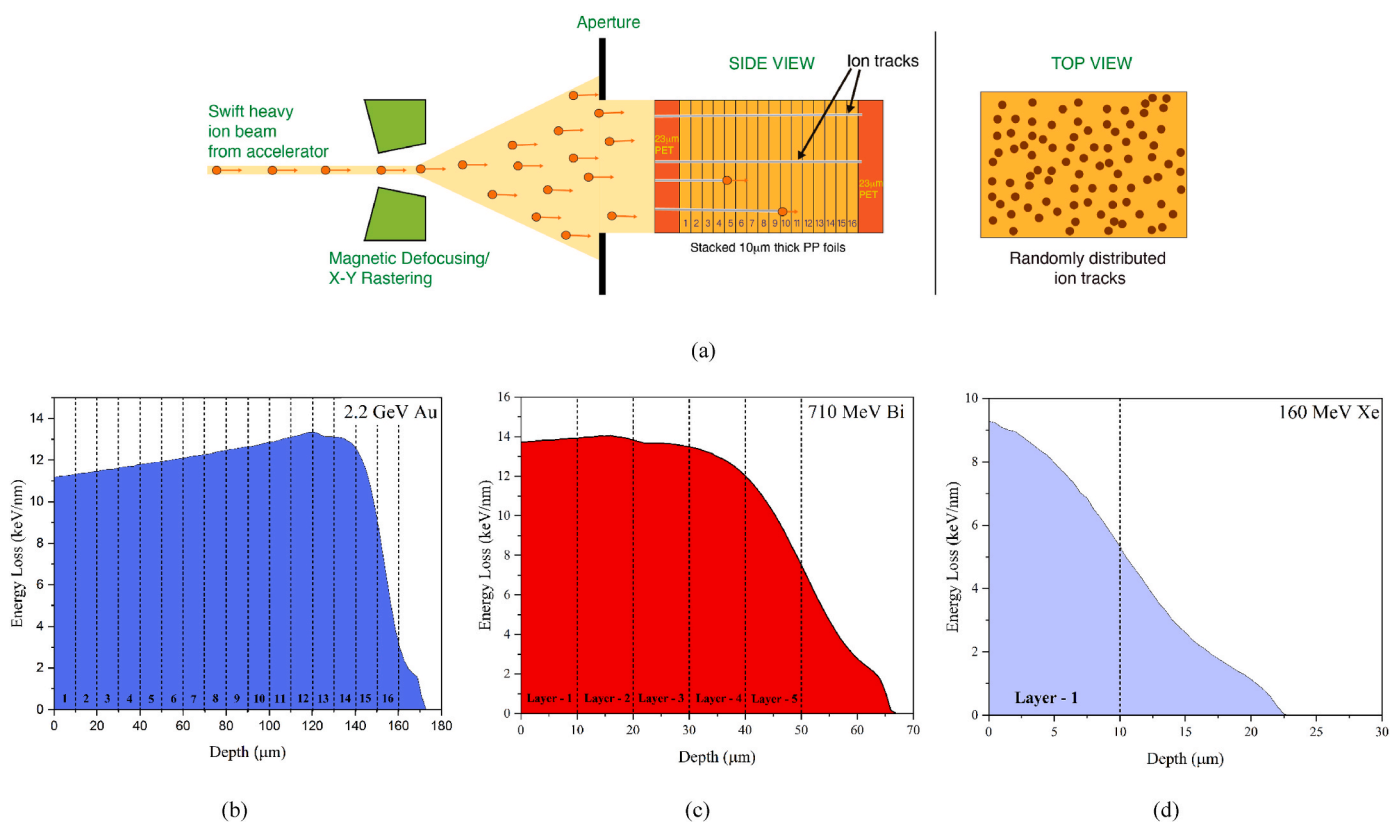**Fig. 1.** UV spectra of foil types T2372 and T2400. Peaks <300 nm wavelength correspond to the presence of hindered phenols in the foils which act as antioxidants. The foil type T2372 clearly has higher concentration of antioxidants than the foil type T2400.

Table 1
Sample Information and irradiation parameters.

Foil type	Antioxidant Content	Thickness	Ion type	Ion energy	Accelerator	Month and Year of Irradiation	Electronic energy loss at the surface of first foil (keV/nm)
T2372	High (~5× as compared to T2400)	10 μm	Au	2250 MeV	UNILAC Accelerator, GSI, Germany	March 1997	13.7
			Bi	710 MeV	U-400 Cyclotron, FLNR JINR, Russia	March 2020	14.1
			Xe	160 MeV	IC-100 Cyclotron, FLNR JINR, Russia	January 2020	9.3
T2400	Low		Au	2250 MeV	UNILAC Accelerator, GSI, Germany	March 1997	13.7
			Bi	710 MeV	U-400 Cyclotron, FLNR JINR, Russia	March 2020	14.1
			Xe	160 MeV	IC-100 Cyclotron, FLNR JINR, Russia	January 2020	9.3

Fig. 2. (a) Schematic illustrating the ion-irradiation of polypropylene stack. PP foil stack has been placed between 23 μm thick PET foils to provide rigidity during the irradiation process. Electronic energy loss of 2.2 GeV Au ions (b), 710 MeV Bi ions (c) and 160 MeV Xe ions (d) in polypropylene foils as a function of penetration depth, as calculated using SRIM code [53]. During irradiation, polypropylene foils of 10 μm thickness were kept in a stack and the layer numbers are indicated in the graphs. The impact of PET foil has been considered in the energy loss values.

and ∼273 nm [51]. Hindered phenols are phenols with one or more functional groups such as tertiary butyl and are used as antioxidants in polymer foils to minimise the oxidative degradation. They are known to be free radical scavengers and have the capacity to donate hydrogen atoms to polymeric radicals in order to stop the oxidation-degradation cycle [52]. When compared to foil type T2400, foil type T2372 shows a greater concentration of these hindered phenols (see Fig. 1) which is directly correlated with a higher concentration of antioxidants.

For both foil types, the irradiation conditions are listed in Table 1. We investigated samples irradiated with 2.2 GeV Au ions 25 years ago (noting that all small-angle X-ray scattering measurements were completed in March 2022) to evaluate the impact of ion track ageing and oxygen absorption over time (especially for the PP foils with lower antioxidant content), as shown in Table 1. The Xe and Bi irradiations were performed in 2020. The Au ion irradiation was performed at the UNILAC accelerator at GSI Helmholtz Centre for Heavy Ion Research in Germany while the Bi and Xe irradiations were carried out at the U-400 cyclotron and the IC-100 cyclotron, respectively, at the Flerov Laboratory of Nuclear Reaction, Joint Institute for Nuclear Research, Russia. For the samples measured using SAXS, the fluences ranged from 3×10^9 to 1×10^{10} ions cm^{-2}. For the irradiation experiments, several foils were stacked on top of each other (referred to as layer 1, layer 2, and so on in this study), leading to different average electronic energy losses in the different layers. For 2.2 GeV Au ion irradiation, 16 polypropylene foils were layered; 5 foils were stacked for 710 MeV Bi ion irradiation, and a single foil was employed for 160 MeV Xe irradiation. A 23 μm PET foil was placed in front of the polypropylene foil stack during irradiation with the Au ions. The effect of the presence of the PET foil has been considered for the energy loss calculations. The electronic energy loss (dE/dx) at the surface of the first foil reported in Table 1 was calculated using the SRIM code [53]. The calculated energy loss as a function of

penetration depth is shown in Fig. 2 for irradiation with 2.2 GeV Au ions (a), 710 MeV Bi ions (b) and 160 MeV Xe ions (c). The reader should note that it has been reported in previous studies that the electronic energy loss (dE/dx) values given by the SRIM code are at least 10% lower as the SRIM algorithm underestimates the energy losses of irradiation with ions of higher atomic numbers in light targets such as polypropylene and similar polymers [46,54].

2.2. Measurements of mass and infrared spectra of PP samples

Samples 5 × 5 cm in size were weighed on an analytical balance (Mettler Toledo XP205) before and after ion irradiation. The irradiation with Bi and Xe ions was performed using homogeneously scanned beams so that the uncertainty in ion fluences did not exceed ±10%. The masses were found to be reproducible for samples equilibrated at room atmosphere within ±0.00002 g. Infrared spectra of pristine and ion-irradiated PP samples were measured in the transmission mode using a Specord M80 instrument (Carl Zeiss Jena). Polypropylene foil layers were stacked between two KBr plates. Paraffinic oil was used as immersion liquid to avoid light scattering and suppress interference pattern.

2.3. Small-angle X-ray scattering measurements and modelling

Transmission SAXS measurements were used to investigate the tracks in polypropylene. The measurements were performed at the SAXS/WAXS beamline of the Australian Synchrotron. The distance between the irradiated polypropylene foils and the detector (Pilatus 2 M) was 3335.5 mm. For the measurements, we employed X-rays with energy of 12 keV corresponding to a wavelength of 1.03 Å. For alignment of the tracks with respect to the X-ray beam, samples were mounted on a
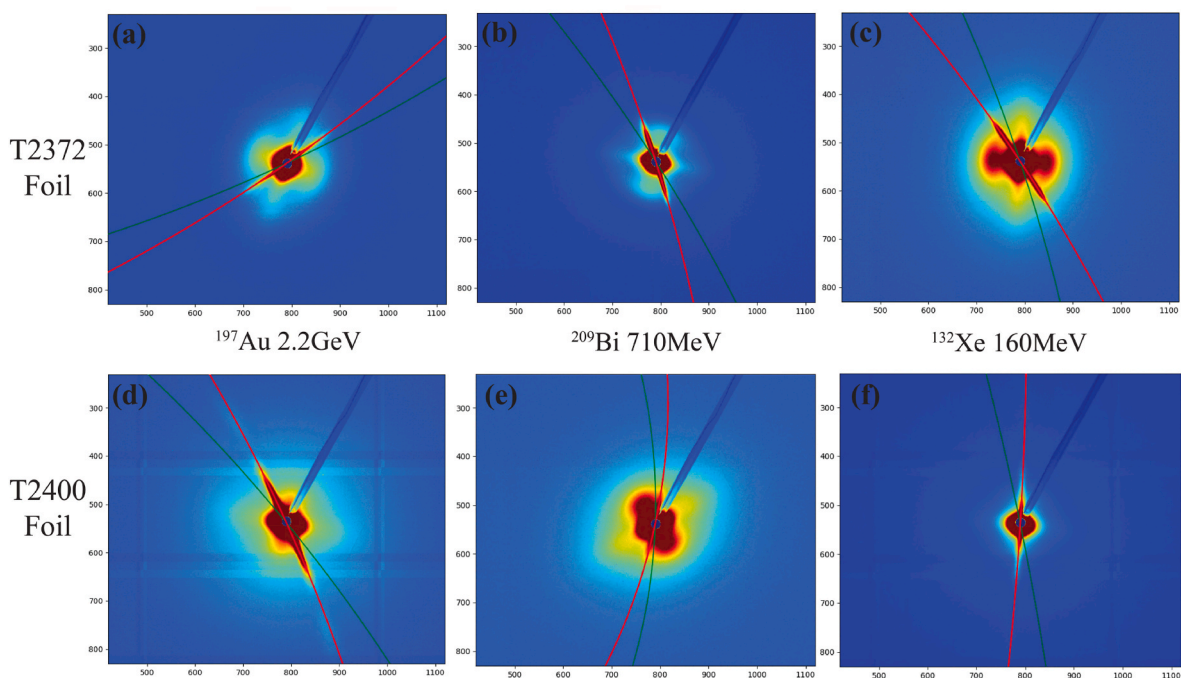
Fig. 3. Two-dimensional scattering patterns originating from the two different kinds of polypropylene foils (T2372: (a) to (c) and T2400: (d) to (f)) irradiated with different ions. The samples and hence the ion track axis was tilted at an angle of approximately 5°–10° with respect to the incoming X-ray beam. The foils were irradiated with 2.2 GeV Au ions (a) and (d), 710 MeV Bi ions (b) and (e) and 160 MeV Xe ions (c) and (f). The central part of the detector is protected against the primary beam using a beam stop. The blob in the middle of the scattering patterns relates to the undamaged PP structure.

three-axis goniometer. When the ion tracks are tilted by approximately 5° and 10° with respect to the incoming X-ray beam, the two-dimensional scattering pattern obtained shows a highly anisotropic pattern of narrow curved streaks resulting from the high aspect ratio of the ion tracks. The two-dimensional scattering patterns obtained for PP films irradiated with different ions are shown in Fig. 3. Fig. 3 (a)–(c) show the scattering patterns for polypropylene foil T2372 irradiated with 2.2 GeV Au (a), 710 MeV Bi (b) and 160 MeV Xe (c). Similarly, scattering patterns for polypropylene foil T2400 irradiated with 2.2 GeV Au (d), 710 MeV Bi (e) and 160 MeV Xe (f) are shown. For analysis, the two-dimensional scattering images were reduced to a one-dimensional scattering intensity patterns by conducting azimuthal integration along the streak employing a thin mask (represented by solid red line) of 2–5 pixels, followed by background removal with a mask of the same

width (represented by solid green line) away from the streak [11,50]. Following data reduction, we use different theoretical models to fit the scattering curves. Further details of the experimental procedure related to SAXS can be found in references [11,47,49,50,55].

Small angle X-ray scattering measures changes in electronic density which is directly related to the atomic density. For fitting of the scattering intensities, we used two form factor models that assume a cylindrical shape of the tracks. The models consider the radial density profile in the cylindrical tracks. We have recently demonstrated that the 'Core Transition Model', may be used to obtain a detailed understanding of the ion track structure in polymers [49]. This model is based on the assumption of a severely damaged cylindrical core with a gradual density transition towards the surrounding undamaged material. We also employ the 'Core Transition Shell Model' for fitting some of the
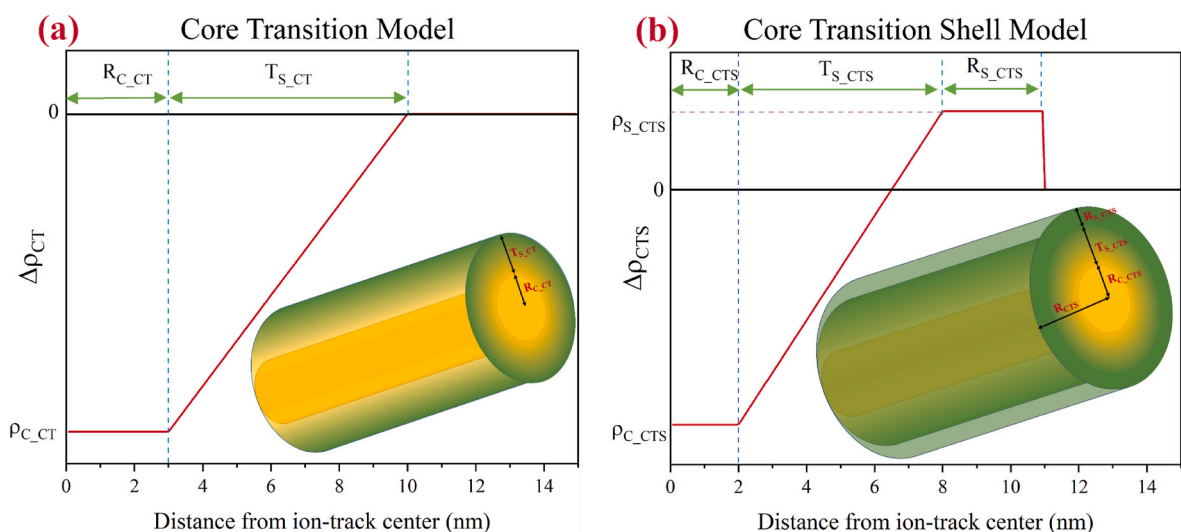
Fig. 4. Diagram showing the radial density variation for the case of (a) the Core Transition Model and (b) the Core Transition Shell Model.

scattering patterns from foil type T2400. This model assumes an under/over-dense core region and over/under-dense shell region connected by a gradual transition between the two [50]. It is not possible to determine whether the core/shell is under/over-dense, or vice versa, just by fitting the scattering intensities with the Core Transition Shell Model; however, such interpretation can be made using other measurement or simulation techniques in addition to SAXS, such as mass measurements of the polymer foils before and after irradiation and molecular dynamic simulations [47]. In the present study, we employ mass measurements in addition to SAXS to determine if the core and shell region are over/under dense compared to the matrix material. Generally, in polymers, due to the formation of volatile radiolysis products and extensive damage following the swift heavy ion irradiation, the track core is usually under-dense compared to the matrix. Fig. 4 illustrates the radial density variation for the Core Transition Model (a) and the Core Transition Shell Model (b).

The scattering amplitude $f(q)$ for the radial density distribution for the Core Transition Model can be expressed as

$$
\begin{aligned}
f_{CT}(q) = 2\pi \, \frac{\sin\left(q_z L/2\right)}{q_z/2} \cdot \frac{\pi}{2q_r^2 T_{S\_CT}} \cdot \big[& R_{C\_CT} \boldsymbol{J_1}(q_r R_{C\_CT}) \boldsymbol{H_0}(q_r R_{C\_CT}) \\
& - (R_{C\_CT} + T_{S\_CT}) \, \boldsymbol{J_1}(q_r(R_{C\_CT} + T_{S\_CT})) \boldsymbol{H_0}(q_r(R_{C\_CT} + T_{S\_CT})) \\
& - R_{C\_CT} \, \boldsymbol{J_0}(q_r \, R_{C\_CT}) \boldsymbol{H_1}(q_r R_{C\_CT}) + (R_{C\_CT} + T_{S\_CT}) \, \boldsymbol{J_0}(q_r(R_{C\_CT} \\
& + T_{S\_CT})) \boldsymbol{H_1}(q_r(R_{C\_CT} + T_{S\_CT})) \big]
\end{aligned}
$$

Eq. 1

where L is length of the ion track and is equal to the thickness of the polymer film. $\boldsymbol{J_0}$ and $\boldsymbol{J_1}$ are the Bessel functions of zero-order and first order, respectively, and $\boldsymbol{H_0}$ and $\boldsymbol{H_1}$ are the Struve functions of zero-order and first-order, respectively. q_r and q_z are the radial and z-component of the scattering vector and can be expressed as $q \cos \theta$ and $q \sin \theta$ respectively where θ is the half scattering angle [11]. R_{C_CT} is the radius of the core region of the ion track characterised by a constant density ρ_{C_CT}. Surrounding the core region, we consider a transition region (T_{S_CT}) and is represented by a linear density change from the core region to the bulk of the material as illustrated in Fig. 4(a). We define the effective radius of the track as $R_{CT} = R_{C\_CT} + T_{S\_CT}/2$, i.e., equivalent to the distance from the centre of the track to the point where the density difference is half of the total density change.

Similarly, the scattering amplitude $f(q)$ for the radial density distribution for the Core Transition Shell Model (see Fig. 4(b)) can be expressed as:

$$
\begin{aligned}
f_{CTS}(q) = 2\pi \, \frac{\sin\left(q_z L/2\right)}{q_z/2} \cdot \frac{1}{2q_r^2 T_{S\_CTS}} \cdot \big[& 2q_r T_s (R_{C\_CTS} + T_{S\_CTS} \\
& + R_{S\_CTS}) \boldsymbol{J_1}(q_r(R_{C\_CTS} + T_{S\_CTS} + R_{S\_CTS})) + \pi(\rho_{CTS} - 1)(\\
& - R_{C\_CTS} \boldsymbol{J_1}(q_r R_{C\_CTS}) \boldsymbol{H_0}(q_r R_{C\_CTS}) + (R_{C\_CTS} \\
& + T_{S\_CTS}) \boldsymbol{J_1}(q_r(R_{C\_CTS} + T_{S\_CTS})) \boldsymbol{H_0}(q_r(R_{C\_CTS} + T_{S\_CTS})) \\
& + R_{C\_CTS} \boldsymbol{J_0}(q_r R_{C\_CTS}) \boldsymbol{H_1}(q_r R_{C\_CTS}) - (R_{C\_CTS} + T_{S\_CTS}) \boldsymbol{J_0}(q_r(R_{C\_CTS} \\
& + T_{S\_CTS})) \boldsymbol{H_1}(q_r(R_{C\_CTS} + T_{S\_CTS}))) \big]
\end{aligned}
$$

Eq. 2

we fit the parameter ρ_{CTS} corresponding to the ratio of the density of the core region (ρ_{C_CTS}) to that of the shell region (ρ_{S_CTS}). Hence, if the ratio is negative, the core and shell regions will have opposing densities, i.e., if the core region is under-dense, the shell region will be over-dense, and vice versa. On the other hand, if the ratio is positive, both core and shell regions will either be over-dense or under-dense compared to the matrix.

Ion-tracks resulting from mono-energetic ion irradiation are generally highly monodisperse and thus have a very narrow size distributions, as highlighted in previous investigations [11,49,50]. To account for the small changes, which may be due to factors such as energy straggling and range straggling caused by electronic and nuclear collisions, we implement a narrow Schulz-Zimm distribution during fitting, which is very similar to a Gaussian distribution for small dispersity values but is always positive, i.e., no non-physical, negative track-radii occur when calculating the scattering pattern. Additionally, while calculating the scattering intensity using the form factor models described above, the assumption is that the ion-tracks are perfectly parallel to each other, but in reality, this is not the case. This small deviation can be due to the small angular dispersion of the incoming swift heavy ions during ion irradiation, but it might also be due to the foils not being exactly flat during the irradiation experiments and/or SAXS measurements. To account for that, we implement a narrow angular distribution that models these variances while fitting the scattering data. For further detail on the implementation of both the size and angle distributions, the reader is directed to our previous work [11,49,50]. Hence, after the implementation of both size and angular distributions, we fit the scattering intensities obtained experimentally using both models defined above.

To further compare the tracks in different polypropylene films and tracks fabricated by different ions, we calculate the absolute density change in the tracks. For finding the absolute density change, we need to do calibration of the absolute scattering intensity using a known standard. We performed the calibration using a glassy carbon standard (thickness 1 mm; often used as a standard as it shows a nearly consistent scattering plateau throughout a wide q range with a known scattering intensity [56]) at various exposure times. The absolute density change from the small-angle X-ray scattering experiments can be obtained by considering $\lim_{q\to 0} I(q)$. The value $I(q\to 0)$ is obtained by extrapolating the fitted scattering curve to very small q values and the absolute density change is calculated following the relationship between the X-ray scattering length density β and the density variations within the ion-track: $\frac{\rho}{\rho_{\text{bulk}}} = \frac{\beta}{\beta_{\text{bulk}}}$ [50]. The corresponding absolute SAXS intensity (for $q\to 0$) for the Core Transition Model can be written as:

$$
I_{CT}(q \to 0) = \frac{1}{9} N L^2 \rho_{C\_CT}^2 \pi^2 \left(3R_{C\_CT}^2 + 3R_{C\_CT}T_{S\_CT} + T_{S\_CT}^2\right)^2
$$

Eq. 3

where N is the number of tracks measured during the experiment. Similarly, the absolute SAXS intensity (at $q\to 0$) for the Core Transition Shell Model can be written as:

$$
I_{CTS}(q \to 0) = N \frac{\pi^2 L^2}{T_{S\_CTS}^2} \rho_{S\_CTS}^2 \left(T_{S\_CTS}(R_{C\_CTS} + T_{S\_CTS} + R_{S\_CTS})^2 + \frac{T_{S\_CTS}}{3}(\rho_{CTS} - 1)\left(3R_{C\_CTS}^2 + 3R_{C\_CTS}T_{S\_CTS} + T_{S\_CTS}^2\right) \right)^2
$$

Eq. 4

where parameters $L, q_r, q_z, \boldsymbol{J_0}, \boldsymbol{J_1}, \boldsymbol{H_0}$ and $\boldsymbol{H_1}$ have the same definition as in Eq. (1). The parameters R_{C_CTS} and R_{S_CTS} define the core region and the shell region respectively. The transition region (T_{S_CTS}) corresponds to a linear density change between the core region and the shell region. The total radius of the track is defined as $R_{CTS} = R_{C\_CTS} + T_{S\_CTS} + R_{S\_CTS}$. During the fitting process using the Core Transition Shell Model,

Using equations (3) and (4) and substituting the values of all the parameters from the fit results, one can calculate the absolute density change respectively for the Core Transition and Core Transition Shell Model.
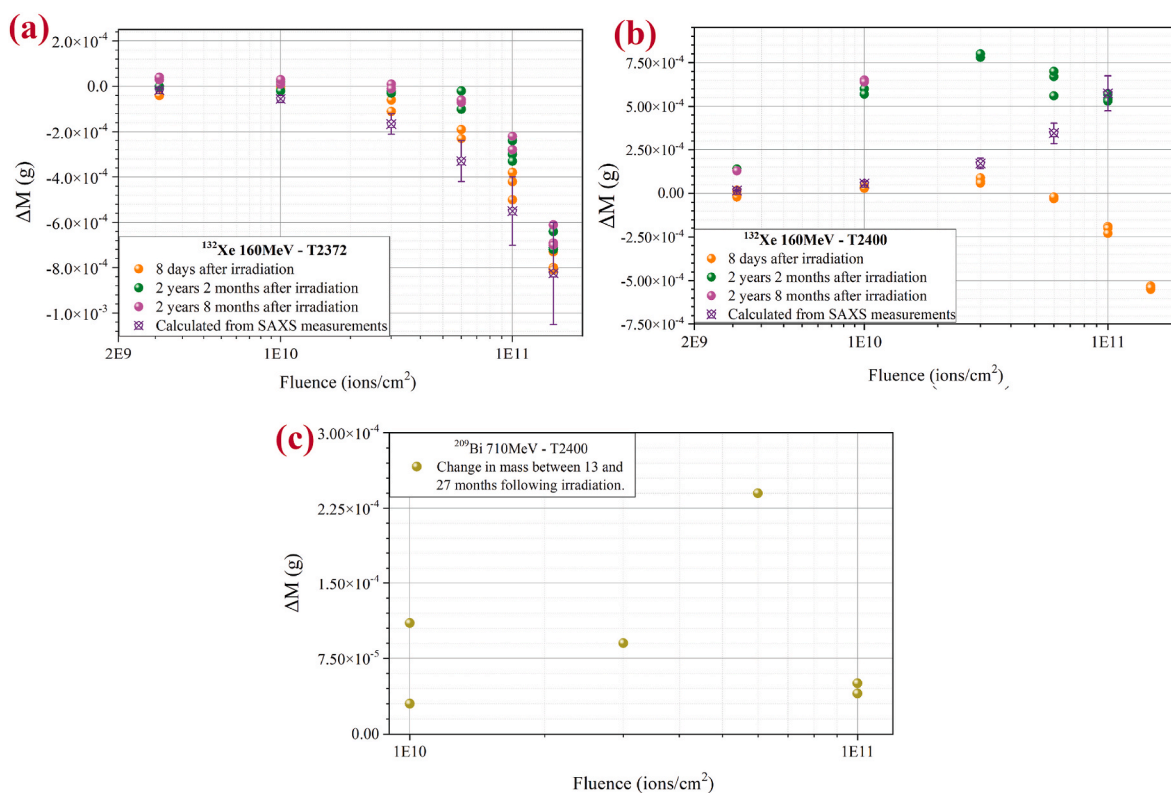
Fig. 5. Change in the mass of the PP foils (size 50 × 50 mm^2) measured and calculated from SAXS measurements after irradiation as a function of fluence for foil type T2372 (a) and T2400 (b) irradiated with ^{132}Xe ions of energy 160 MeV. (c) The change in mass between 13- and 27-months following irradiation for foil type T2400 irradiated with ^{209}Bi ions of energy 710 MeV.
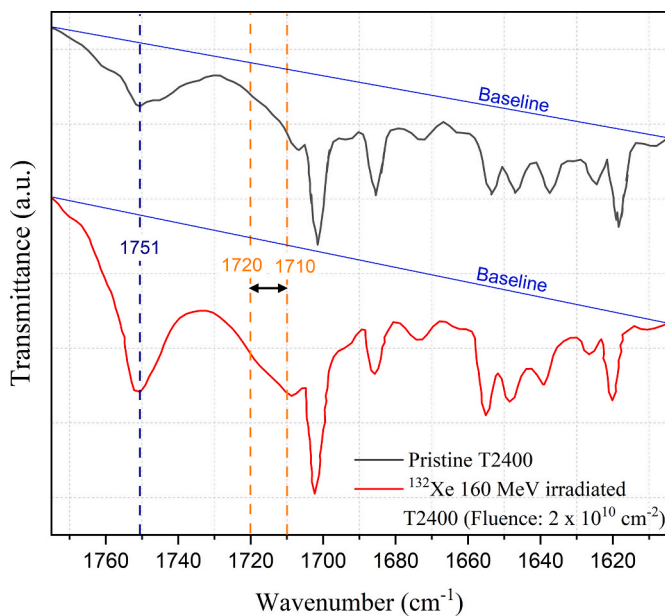
Fig. 6. Infrared transmission spectra of polypropylene samples: pristine PP foil with low content of antioxidant (T2400) (solid black line); the PP foil irradiated with a Xe ion fluence of 2×10^{10} cm^{-2} (solid red line). Spectra shown for irradiated PP foils was recorded 26 months after irradiation. (For interpretation of the references to colour in this figure legend, the reader is referred to the Web version of this article.)

3. Results and discussion

3.1. Mass change of foils

It is well known that molecules from the polymer are ejected into the gas phase upon swift heavy ion irradiation. Free radicals are also produced as a result of chain scissions and atom as well as side group abstraction, which are caused by the irradiation. Particularly in polymers, bond breaking, and outgassing dominate the process of ion track formation in the track core, generally resulting in a reduction in the mass of the foil following exposure to swift heavy ion irradiation [57,58]. Additionally, there is a halo damage surrounding the track core as well with much larger radius (exceeding 100 nm for some polymers) but without significant mass loss. Here, we examined the weight of several samples of both types of foils, i.e. T2372 and T2400, before and after irradiation, in order to quantify the impact of the antioxidants on the irradiation damage. After the ion exposure, the samples were weighed at different time intervals to determine how their mass changed over time.

The change in mass of PP foils of size (50 mm × 50 mm) as a function of fluence has been plotted in Fig. 5. Fig. 5 (a) and (b) show the change in the mass of the foil type T2372 and T2400, respectively, following Xe irradiation, measured at three different intervals i.e., (i) 8 days, (ii) 2 years and 2 months and (iii) 2 years and 8 months after irradiation. The change in mass calculated from the SAXS measurements is also plotted and discussed in the next subsections. It is evident that for foil type T2372, the mass decreases after irradiation, and that this change increases with increasing fluence. The measurements taken 8 days after the irradiation show the largest decrease. We found a minor but discernible increase in mass when the foils were measured 2 years, 2 months, and 2 years, 8 months after irradiation. Nevertheless, a general decrease in the mass of the foils was seen for all the measurements as expected due to outgassing in the highly damaged track-core region. These results also indicate that for the foil with high antioxidant content,

6

the effect of aging is not very pronounced. On the other hand, for the foil type T2400, a reduction in mass was seen when measurements were taken 8 days after the irradiation and the trend looked quite similar to the foil type T2372. However, when measurements were repeated 2 years and 2 months later, a clear increase in the mass of the foils was seen, which may indicate a high level of free radical oxidation.

Post-irradiation oxidation of polypropylene and other polyolefines is a well-known phenomenon which has been studied using a variety of spectroscopy methods [59–61]. In order to confirm oxidation of PP in tracks after irradiation, we employed conventional infrared spectroscopy. Fig. 6 shows the spectra of a pristine T2400 PP sample (a) and an irradiated (160 MeV Xe, fluence = 2×10^{10} cm^{-2}) T2400 PP sample (b). Spectra (b) was recorded 26 months after irradiation. Absorption bands in the region between 1700 and 1760 cm^{-1} clearly show the formation of oxygen-containing species in the ion tracks. The decrease in transmittance (rise of absorption) at 1710-1720 cm^{-1} is associated with carbonyl groups in the acid dimeric form and/or ketones or aldehydes [60]. A free acid and/or ester form can be assigned to the absorption band at 1751 cm^{-1} [60].

To better understand what happens to the polymer around the track after ion impact, we should consider the uptake of oxygen on the molecular level. The mass increase for the Xe-irradiated T2400 sample (Fig. 5(b), fluence of 1×10^{10} cm^{-2}) of ~5.9×10^{-4} g corresponds to 1.1×10^{19} oxygen molecules per sample 25 cm^2 in area. Therefore,

approximately 4.4×10^7 O$_2$ molecules are absorbed in one track, which corresponds to 4400 O$_2$ molecules per 1 nm of track length. The average energy loss of Xe ions in the PP foil is ~7 keV/nm. Thus, the radiation chemical yield (the number of molecules formed or consumed when the system absorbs 100 eV radiation energy) of oxygen uptake G (O$_2$ uptake) $\approx$ 63. Since the yield of primary radicals in PP is on the order of several units [62], it is clear that the observed mass increase is possible due to oxidative chain reaction. Hence, the primary radicals produced due to irradiation, capture the oxygen molecule which leads to the formation of peroxide radicals. Through the abstraction of hydrogen from macromolecules the peroxide radicals are transformed into hydroperoxides, hydroperoxides then decay into new primary radicals and the whole process is repeated again [59,63]. Additionally, it was observed that the mass decreases at high fluences ($>3 \times 10^{10}$ ions/cm^2). Irradiation with high fluence leads to a large concentration of free radicals which subsequently recombine and lead to less absorption of oxygen overall. This could be the reason for the observation of a reduction of mass at high fluences. We once again noticed a further increase in mass when the change in mass was assessed again after another six months. This observation was also accompanied by the fact that the samples become more and more brittle with age following irradiation. As a consequence, 2 years and 8 months after the irradiation, we were unable to measure the change in mass for all the samples.

We did not measure the initial mass of the foils which were irradiated
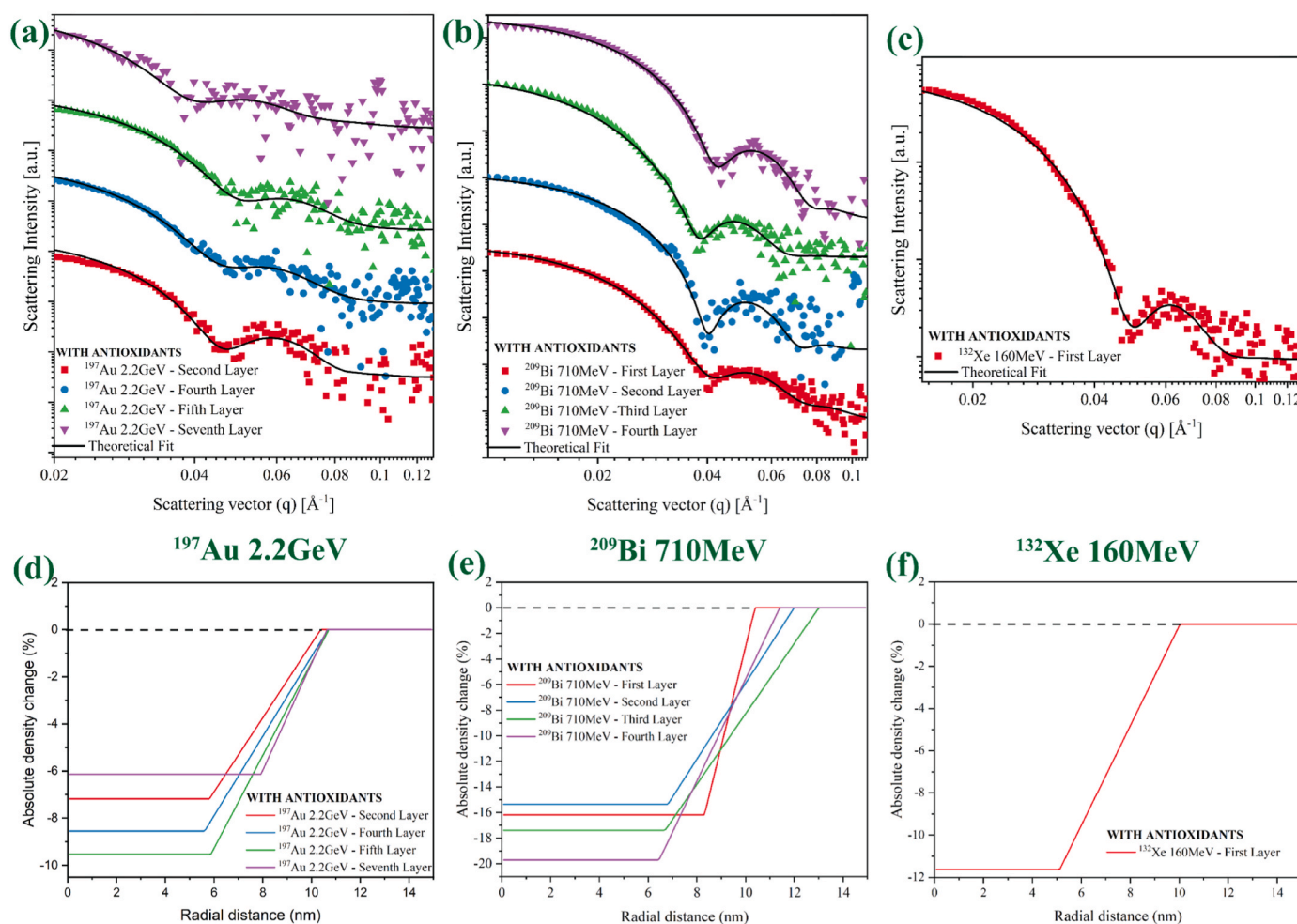
Fig. 7. Integrated SAXS scattering intensities for ion tracks in polypropylene foil type T2372. The solid black lines in each graph represents the fit obtained using the Core Transition Model. Graphs (a) through (c) show the experimental data and fits for ion tracks generated by irradiation with different ions of varying energy (different layers). Graphs (d) through (f) show the corresponding absolute radial electronic density profile of ion tracks, calculated numerically using parameters that were determined by fitting the experimental scattering curves. For better visualisation, the scattering patterns in graphs (a) and (b) are offset on the y-axis.
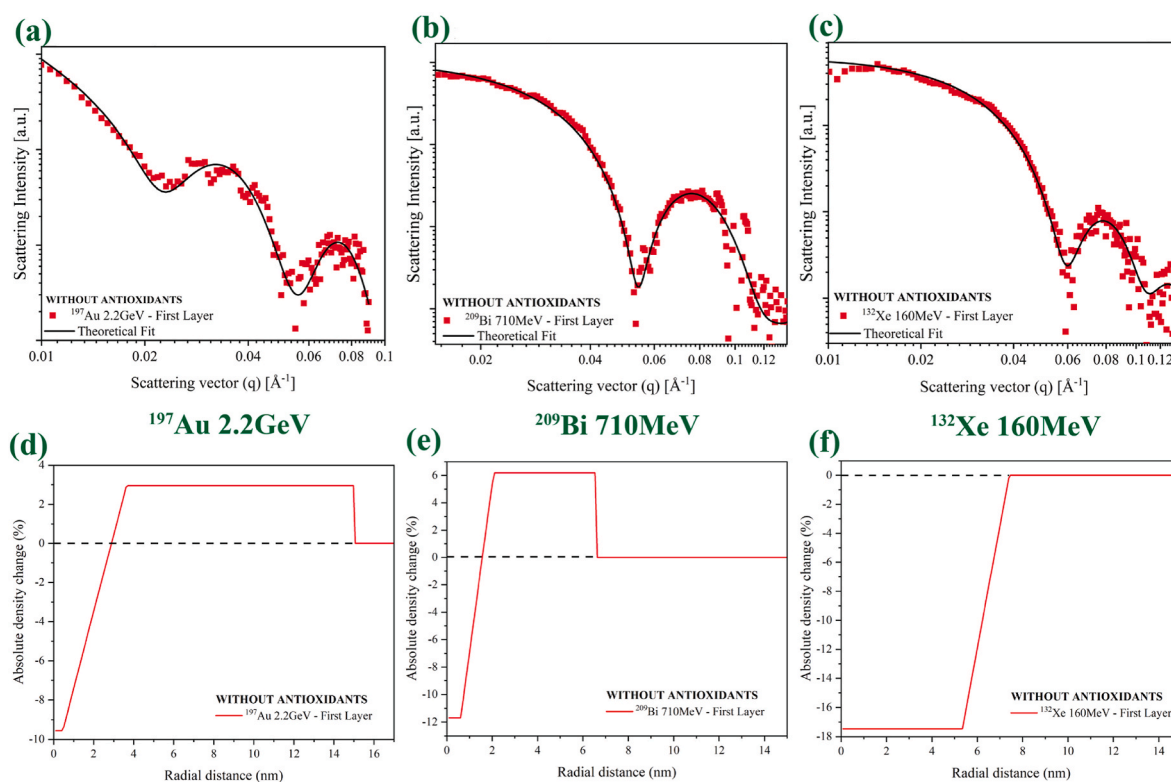
Fig. 8. Integrated SAXS scattering intensities for ion tracks in polypropylene foil type T2400. The solid black lines in each graph represents the fit obtained using either the Core Transition Model or the Core Transition Shell Model. Graphs (a) through (c) show the experimental data and fits for ion tracks generated by irradiation with different ions of varying energy. Graphs (d) through (f) show the corresponding absolute radial electronic density profiles of ion tracks, calculated numerically using parameters that were determined by fitting the experimental scattering patterns.

Table 2
Fitting parameters from SAXS measurements for different polypropylene foils using the Core Transition Model and the Core Transition Shell Model. The radii given for the Core Transition Model refer to the effective ion track radius, which is defined as the sum of core radius and half of the transition region. The radii given for the Core Transition Shell Model are equal to the sum of core, transition and shell region. In the cases of the Core Transition Model and the Core Transition Shell Model, respectively, the radial dispersity values are reported as a percentage of the values of the core region and the transition region.

Foil details	Ion type, ion energy and Fluence	Layer	Form Factor Model used for fitting	Core (nm)	Transition (nm)	Shell (nm)	Radius (nm)	Radial Dispersity (percentage)
T2372 (High Antioxidant Content)	Au, 2250 MeV, 1×10^{10} ions/cm^2	2nd Layer	Core Transition Model	5.81 ± 0.32	4.56 ± 0.57	–	8.09 ± 0.43	$9.8\% \pm 5.5\%$
		4th Layer		5.61 ± 0.34	5.06 ± 0.51	–	8.14 ± 0.42	$14.6\% \pm 2.4\%$
		5th Layer		5.87 ± 0.32	4.83 ± 0.64	–	8.29 ± 0.45	$13.1\% \pm 1.9\%$
		7th Layer		7.92 ± 0.92	2.71 ± 1.52	–	9.28 ± 1.19	$13.8\% \pm 5.1\%$
	Bi, 710 MeV, 1×10^{10} ions/cm^2	1st Layer		8.31 ± 0.21	2.08 ± 0.44	–	9.35 ± 0.30	$14.1\% \pm 2.9\%$
		2nd Layer		6.81 ± 0.59	5.18 ± 1.05	–	9.39 ± 0.79	$8.5\% \pm 4.1\%$
		3rd Layer		6.69 ± 0.37	6.32 ± 0.65	–	9.85 ± 0.49	$6.1\% \pm 2.4\%$
		4th Layer		6.45 ± 0.45	4.95 ± 0.87	–	8.93 ± 0.63	$7.5\% \pm 1.4\%$
	Xe, 160 MeV, 1×10^{10} ions/cm^2	1st Layer		5.12 ± 0.23	4.92 ± 0.41	–	7.58 ± 0.31	$7.8 \% \pm 1.2\%$
T2400 (Low Antioxidant Content)	Au, 2250 MeV, 3×10^{9} ions/cm^2	1st Layer	Core Transition Shell Model	0.45 ± 0.24	3.19 ± 0.27	11.38 ± 0.31	15.02 ± 0.43	$13.5\% \pm 2.1\%$
	Bi, 710 MeV, 3×10^{9} ions/cm^2	1st Layer		0.61 ± 0.41	1.46 ± 1.39	4.48 ± 1.09	6.55 ± 1.81	$4.3\% \pm 2.5\%$
	Xe, 160 MeV, 1×10^{10} ions/cm^2	1st Layer	Core Transition Model	5.35 ± 0.33	2.06 ± 0.64	–	6.38 ± 0.46	$7.8\% \pm 1.2\%$
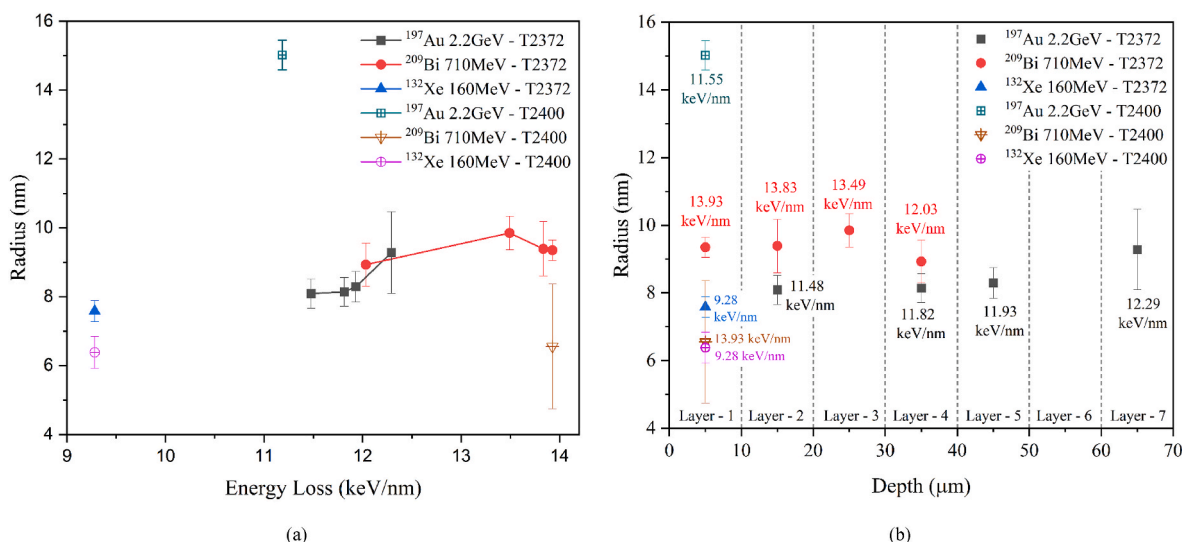
Fig. 9. Total/effective radius as a function of electronic energy loss (a) and depth (b) for different irradiation conditions for both the foil types. For the case of foil type T2372 – with high antioxidant content, it can be clearly seen that the effective radii obtained from fitting the scattering data, increase with increasing energy loss. The energy losses reported for both cases refer to the values at the surface of the foil.

with ^{209}Bi ions with 710 MeV energy, but a change in mass between 13 and 27 months following irradiation was measured and a clear increase in the mass of the foils of type T2400 was observed (see Fig. 5(c)). Although these measurements clearly show that oxidation maybe a significant component, particularly for foils with low antioxidant content, and that oxidation increases over time, it is challenging to determine how much oxygen the polymer consumes. While the mass increase is an indication of oxidation, it cannot entirely be discounted that the absorption of oxygen from the atmosphere does not accompany/result in the emission of other gaseous products.

3.2. Structure of ion tracks in foil type T2372

To measure the structure of the ion tracks and how they are affected

by the presence of antioxidants in the foils, we measured different samples using small angle X-ray scattering. As mentioned earlier, SAXS measurements were done ~25 years after irradiation for Au irradiated samples and ~2 years and 2 years - 2 months after irradiation for Bi and Xe irradiated samples respectively. It was not possible to get scattering intensities with sufficient signal-to-noise ratios from all layers, in particular from those samples with low irradiation fluences (3×10^9 ions cm^{-2}). As a result, in this study, we are only reporting the findings from data that have a reasonable signal-to-noise ratio and can be relied upon. A Python and C-based program that implemented a non-linear least-square fitting algorithm was used to fit the 1D scattering data that was obtained after data reduction of 2D scattering patterns as explained in section 2.3. The one-dimensional scattering patterns obtained along with the fits and the corresponding absolute radial density

Table 3

The absolute density changes for the core region and the ratio of the density of the core region to that of the shell region (for the case where fitting has been done using Core Transition Shell Model) and corresponding mass change per ion track for different samples. The positive and negative sign in front of mass change results indicates an increase and decrease in the mass respectively. This hypothesis is based on the experimental observation of an increase/decrease of mass of foils before and after irradiation.

Foil details	Ion type, ion energy and Fluence	Layer	$\rho_{CTS} = \dfrac{\rho_{C\_CTS}}{\rho_{S\_CTS}}$	Absolute density change for the Core region (%)	Mass change per ion track (10^{-16} g)
T2372 (High Antioxidant Content)	Au, 2250 MeV, 1×10^{10} ions/cm^2	2nd Layer	–	7.1% ± 1.9%	− 1.5 ± 0.4
		4th Layer	–	8.6% ± 2.3%	− 1.8 ± 0.5
		5th Layer	–	9.5% ± 2.5%	− 2.1 ± 0.6
		7th Layer	–	6.2% ± 2.2%	− 1.7 ± 0.7
	Bi, 710 MeV, 1×10^{10} ions/cm^2	1st Layer	–	16.2% ± 2.7%	− 4.5 ± 0.8
		2nd Layer	–	15.3% ± 3.6%	− 4.4 ± 1.3
		3rd Layer	–	17.4% ± 3.9%	− 5.5 ± 1.6
		4th Layer	–	19.8% ± 5.4%	− 5.1 ± 1.6
	Xe, 160 MeV, 1×10^{10} ions/cm^2	1st Layer	–	11.7% ± 3.2%	− 2.2 ± 0.6
T2400 (Low Antioxidant Content)	Au, 2250 MeV, 3×10^9 ions/cm^2	1st Layer	− 3.23 ± 0.45	9.5% ± 3.3%	1.1 ± 0.5
	Bi, 710 MeV, 3×10^9 ions/cm^2	1st Layer	− 1.89 ± 0.27	11.7% ± 4.4%	4.4 ± 1.9
	Xe, 160 MeV, 1×10^{10} ions/cm^2	1st Layer	–	17.47% ± 0.9%	2.3 ± 0.4

profiles obtained from the fit parameters for polypropylene foil type T2372 are shown in Fig. 7. Values for the different parameters obtained from the fits are listed in Table 2. The radial dispersity values in Table 2 are reported as a percentage of the value of the core region and the transition region in the case of the Core Transition Model and the Core Transition Shell Model, respectively as.

These scattering intensity plots and fits for the polypropylene foil T2372, i.e., the foil with higher antioxidant content are shown in Fig. 7 (a), (b) and (c). It is evident from the graphs that the fits accurately reflect the experimental data. The foils were irradiated with a fluence of 1×10^{10} ions/cm^2. The scattering data and fits originating from the second, fourth, fifth and seventh layer of polypropylene stack irradiated with 2.2 GeV Au ions are shown in Fig. 7 (a). The corresponding electronic density distribution profiles are illustrated in Fig. 7 (d). Fig. 9 shows the effective radius (for the case of fitting with the Core Transition Model) or total radius (for the case of fitting with the Core Transition Shell Model) as a function of electronic energy loss (a) and depth (b). The fits for the polypropylene foil with higher antioxidant content were performed employing the Core Transition Model. As apparent in Fig. 9 (a) and (b), we discovered that the effective radius increases as we go deeper in the stack. This behaviour can be attributed to the increasing electronic stopping power as the layer number increases. Additionally, we see that the core radius grows for the seventh layer while almost remaining constant for the second, fourth, and fifth layers. The absolute electronic density changes calculated from the SAXS measurements are reported in Table 3. The absolute density change observed for the samples irradiated with Au ions ranges from ~6% to ~10% in the core for different layers. The density change increases from the second to the fifth layer and then reduces for the seventh layer. We want to emphasise to the reader that whereas the radius obtained from SAXS is very accurate, the density difference values obtained have a high degree of uncertainty, thus we cannot be completely certain of this shift. The uncertainties can be as high as 40% and originate mainly from the extrapolation of intensity values at q = 0.

Fig. 7 (b) and Fig. 7 (e) display the scattering intensities and their numerical fits, and the corresponding radial density profiles, respectively, for ion-tracks produced by irradiation with 710 MeV Bi ions. The graph shows the results of the first four layers of the stack and exceptional fits were obtained using the Core Transition Model. For this case, we observed that the effective radius remains almost the same (within uncertainties) for the first three layers and reduces for the fourth layer as can be seen in Fig. 9. This behaviour is also consistent with the electronic stopping power which remains almost constant for the first three layers and decreases in the fourth layer. The absolute density differences obtained for Bi irradiation show a higher change ranging from ~15% to ~20%. With the exception of the first layer, the density change grows with increasing layer number, but this change is within the uncertainty. Fig. 7 (c) and Fig. 7 (f) show the SAXS scattering curve and obtained fit for the irradiation with 160 MeV Xe ions and the corresponding absolute radial density change profile respectively. An effective radius of 7.6 ± 0.3 nm and an absolute density change of ~12% is observed for this case.

As illustrated in Fig. 9, we found that the Bi irradiation generated the largest tracks when comparing the results with Au and Xe irradiation. The ion tracks resulting from the Bi irradiation also show the greatest change in absolute density. Ion tracks produced with 160 MeV Xe irradiation have the smallest effective radius. These variations can directly be related to the changing ion energy and ion mass and hence the changing electronic stopping power between different irradiations (cf. Fig. 9). We also observe that compared to the ion tracks created by irradiation with Bi and Xe ions (irradiation performed in 2020), oscillations in the SAXS scattering intensities obtained for the PP foils irradiated with Au ions in 1997 are weaker and smeared out. This could be because these samples were irradiated almost 23 years apart from each other and the old samples were affected (to a small degree) by the

atmospheric reactions even if they contain higher antioxidant levels. Additionally, the glass transition temperature of the amorphous phase in PP is very close to the room temperature, making it conceivable for molecular rearrangement to occur gradually over the course of the lengthy storage period, which could then result in the observation of weaker scattering intensities.

The mass change per ion track for different samples is also reported in Table 3. The negative and positive signs in front of the mass change values indicate a decrease and an increase in the mass of the foils per ion track, respectively. As previously noted, we cannot directly determine if density change relates to an increase or decrease compared to the material's bulk. However, we use negative and positive signs based on observed mass changes in foils before and after irradiation. We calculate a mass loss per ion track of $(2.2 \pm 0.6) \times 10^{-16}$ g for sample irradiated with 160 MeV Xe ions. The calculated change in mass from SAXS as a function of fluence is also plotted in Fig. 5(a). The mass change per ion track directly correlates to a mass loss of $(5.5 \pm 1.6) \times 10^{-5}$ g and $(1.6 \pm 0.5) \times 10^{-4}$ g for foils of 50 mm × 50 mm size irradiated with Xe ions with a fluence of 1×10^{10} ions cm^{-2} and 3×10^{10} ions cm^{-2} respectively. These results (for all fluences) match well with the experimentally observed mass loss (cf. Fig. 5(a)) in these foils.

3.3. Structure of ion tracks in foil type T2400

Fig. 8 shows the scattering intensities, fits, and the corresponding absolute density profiles for ion tracks generated by irradiation with 2.2 GeV Au, 710 MeV Bi and 160 MeV Xe ions, respectively, in polypropylene foil type T2400, i.e., the foil with a lower concentration of antioxidants. It was more difficult to observe ion tracks using SAXS in the different layers of the stack in PP foil type T2400 than it was with foil type T2372. Hence, we are discussing the results of the first layer of each as we only could reliably extract good data from these samples. Fig. 8 (a) and (d) show the results for ion tracks generated by Au irradiation. As illustrated in the figures, the Core Transition Shell Model was used to fit the data since the Core Transition Model was unable to replicate the experimental scattering intensities. We observed a very small core region (0.45 ± 0.24 nm) of constant density and a larger shell region around the core. The core and shell region are linked by a linear transition region of size 3.19 ± 0.27 nm as can be seen in Fig. 8 (d). The ratio of the electronic density of the core region to that of the shell region was fitted to -3.23 ± 0.45. Negative density ratio indicates that either the core region is under dense and shell region is over density or vice versa. If we consider that the core region is under-dense and the shell region is over-dense, the density profile yields a net increase in the mass of the polymer foil after irradiation. This is consistent with the mass measurements of this foil type (T2400) that show an increase in mass after irradiation. It supports our assumption of significant oxygen absorption as a result of oxidation. Oxygen absorption can be one of the reasons for the increase in the density which ultimately leads to an over-dense region outside the track core and an overall increase in mass as observed. We also hypothesize that the oxidation-related deterioration of ion tracks over time has led to poor signal to noise-ratio. We observe an absolute density change of ~9.5% for the core region and ~3% for the shell region. Considering an under-dense core region and an over-dense shell region, we calculate a mass increase per ion track of $(1.1 \pm 0.5) \times 10^{-16}$ g.

Similarly, for the case of Bi irradiation of PP foil type T2400, we observe that the Core Transition Shell Model provides a superior match to the experimental data. Fig. 8 (b) and (d) illustrate, respectively, the scattering intensity and fit, and the associated absolute radial density profile. Once more, we saw a small core region of size 0.61 ± 0.41 nm. The transition region was found to be of 1.46 ± 1.39 nm while the shell region was found to have the size of 4.48 ± 1.09 nm. The total radius (6.55 ± 1.81 nm) was found to be significantly smaller than the radius of ion tracks resulting from irradiation with Bi in foil type T2372. Bi

irradiation resulted in an absolute density change of approximately 11.7% for the core region and 6.2% for the shell region. As indicated in Table 3, using the assumption similar to the irradiation of foil type T2400 with Au ions, we calculate a mass increase per ion track of $(4.4 \pm 1.9) \times 10^{-16}$ g.

Contrary to the irradiation of foil type T2400 with Au and Bi ions, experimental data originating from ion tracks produced by irradiation with Xe ions was satisfactorily fitted with the Core Transition Model as shown in Fig. 8 (c). The calculated absolute radial density profile is illustrated in Fig. 8 (f). We observe a core region of 5.35 ± 0.33 nm and a transition region of 2.06 ± 0.64 nm. The effective radius observed was 6.38 ± 0.46 nm. This radius is smaller as compared to Xe irradiation of PP foil type T2372. Also, the absolute density change was observed to be ~17.5% as compared to ~11.6% for PP foil type T2372. Even though we do not observe an over-dense shell region for irradiation with Xe ions in PP foil type T2400, the increase in mass observed experimentally can be explained through the oxidation of the halo region. We calculate a mass increase per ion track of $(2.3 \pm 0.4) \times 10^{-16}$ g which correlates to a mass increase of $(5.6 \pm 0.9) \times 10^{-5}$ g and $(1.7 \pm 0.3) \times 10^{-4}$ g for foils of 50 mm × 50 mm size irradiated with Xe ions with a fluence of 1×10^{10} ions cm^{-2} and 3×10^{10} ions cm^{-2} respectively. These values along with other calculated values from SAXS measurements are plotted in Fig. 5 (b). Although these calculations show a much smaller mass change (with highest difference of $(5.4 \pm 0.9) \times 10^{-4}$ g observed for foil irradiated with fluence of 1×10^{10} ions cm^2) than the values observed from weighing (cf. Fig. 5(b)), the disparity may be the consequence of oxygen absorption in a halo region. Due to a very slight density difference from the material's bulk, we cannot detect any halo region using small angle X-ray scattering. Previous studies have shown that the halo zone in polymers can have a size exceeding 100 nm in radius [11,64]. Despite the fact that the dose deposition in the halo region is lower than that of the ion track and decreases radially, it can nevertheless cause enough damage to trigger oxygen absorption. This could account for the observed higher mass increase in foils for the low fluences.

On comparison of all the irradiation conditions for the foil type T2400, we observe a very large radius for the Au irradiated ion tracks as compared to Xe and Bi irradiated samples. This, together with the fact that the masses of the foils keep increasing over time, directly shows that the Au ion tracks progressively broaden over the course of its 25-year lifespan. In addition to the aforementioned details, it's possible that the lack of a shell area in case of samples irradiated with 160 MeV Xe ions was due to the lower energy deposition. The direct observation of the Core Transition Shell structure is made possible by samples that have been exposed to higher energy radiation (such as those exposed to Au and Bi). Oxygen absorption may be greater in these samples in the shell region.

In previous work it was found that PP foils with a higher content of antioxidant show a considerably higher track etch rate [65]. It was hypothesized that this behaviour was associated with the suppression of cross-linking in the tracks. The SAXS data obtained in the present study also allow us to suggest a more plausible hypothesis. As seen from Fig. 7 (d, e, f) and 8 (d, e, f), the tracks in the PP foils with higher antioxidant content have a much greater free volume which is known to be of primary importance for selective etching.

4. Conclusions

In this study, ion tracks in two polypropylene foils with different antioxidant content were characterised using SAXS measurements and the results compared with mass measurements of the polypropylene foils before and after irradiation. The dissipation of the swift ion energy in a polymer occurs in a small volume around the ion path. Further oxidation of the polymer starts within the damage volume and propagates in radial direction towards the polymer bulk. SAXS measurements provides a unique chance to estimate the localization of the oxidative reactions via the measurements of density distribution around in ion tracks.

We found that tracks in foils with higher antioxidant content exhibit a highly damaged core with a mass loss of between 6% and 20%, depending on the ion and energy. The mass loss decreases gradually with increasing distance from the damage core. The structure is comparable to that of other well studied polymers such as polycarbonate, PET and PMMA [49]. For the foils with low antioxidant content, we discovered that the ion tracks have a core shell structure with an overall mass increase which is consistent with an observed increase in mass of these foils after irradiation. Additionally, it was found that the antioxidant content of the film had a significant impact on how quickly the foils degraded over time. The calculated mass increase from the SAXS measurements for polypropylene foil with low antioxidant content is less than the measured increase, whereas the decrease in the mass calculated from SAXS measurements for polypropylene foils with high antioxidant content agrees well with the experimental observation. This suggests that ion irradiation may also lead to the oxidation of the halo area (which is not observable through SAXS), in addition to the oxidation of the ion track (albeit to a lesser amount). The discovery of a tiny core area in foil type T2400 suggests that the core region is heavily oxidised. The oxygen distribution, however, cannot be quantitatively determined since the oxidative degradation phenomenon involves several complicated processes. These findings are crucial because they not only fill in the knowledge gap about the structure of the ion tracks in polypropylene, but they also demonstrate the impact of age, antioxidant content, ion species, and ion energy. Given that polypropylene foil is manufactured in such large quantities, these findings may also be used by material scientists, physicists, and chemists, to build applications based on polypropylene foils.

CRediT authorship contribution statement

Shankar Dutt: Conceptualization, Methodology, Software, Validation, Formal analysis, Investigation, Visualization, Writing – original draft. **Pavel Apel:** Conceptualization, Methodology, Investigation, Formal analysis, Writing – review & editing. **Olga Polezhaeva:** Investigation. **Alexander Kiy:** Investigation. **Nahid Afrin:** Investigation. **Christian Notthoff:** Investigation. **Nigel Kirby:** Investigation. **Patrick Kluth:** Conceptualization, Methodology, Investigation, Resources, Formal analysis, Writing – review & editing, Visualization, Supervision, Funding acquisition.

Declaration of competing interest

There is no conflict of interest.

Data availability

Data will be made available on request.

Acknowledgments

References

[1] E.T. Acar, S.F. Buchsbaum, C. Combs, F. Fornasiero, Z.S. Siwy, Biomimetic potassium-selective nanopores, Sci. Adv. 5 (2019), https://doi.org/10.1126/sciadv.aav2568 eaav2568.

[2] S.P. Adiga, C. Jin, L.A. Curtiss, N.A. Monteiro-Riviere, R.J. Narayan, Nanoporous membranes for medical and biological applications: nanoporous membranes for medical and biological applications, Wiley Interdiscip. Rev. Nanomed. Nanobiotechnol. 1 (2009) 568–581, https://doi.org/10.1002/wnan.50.

[3] S.P. Adiga, D.W. Brenner, Stimuli-responsive polymer brushes for flow control through nanopores, J. Funct. Biomater. 3 (2012) 239–256, 10/gchrss.

[4] P. Apel, Swift ion effects in polymers: industrial applications, Nucl. Instrum. Methods Phys. Res. Sect. B Beam Interact. Mater. Atoms 208 (2003) 11–20, 10/cqpdjk.

[5] P. Apel, Track etching technique in membrane technology, Radiat. Meas. 34 (2001) 559–566, 10/d88tj2.

[6] P.Yu Apel, I.V. Blonskaya, N.E. Lizunov, K. Olejniczak, O.L. Orelovitch, B. A. Sartowska, S.N. Dmitriev, Asymmetrical nanopores in track membranes: fabrication, the effect of nanopore shape and electric charge of pore walls, promising applications, Russ. J. Electrochem. 53 (2017) 58–69, 10/f9tz38.

[7] B. Balannec, A. Ghoufi, A. Szymczyk, Nanofiltration performance of conical and hourglass nanopores, J. Membr. Sci. 552 (2018) 336–340, https://doi.org/10.1016/j.memsci.2018.02.026.

[8] S. Blanco, R. Vargas, J. Mostany, C. Borrás, B.R. Scharifker, Modeling the growth of nanowire arrays in porous membrane templates, J. Electrochem. Soc. 161 (2014) E3341–E3347, 10/f59wsf.

[9] Q. Chen, Z. Liu, Fabrication and applications of solid-state nanopores, Sensors 19 (2019) 1886, 10/ghgqdk.

[10] C. Dekker, Solid-state nanopores, Nat. Nanotechnol. 2 (2007) 209–215, 10/cdf9hc.

[11] S. Dutt, P. Apel, N. Lizunov, C. Notthoff, Q. Wen, C. Trautmann, P. Mota-Santiago, N. Kirby, P. Kluth, Shape of nanopores in track-etched polycarbonate membranes, J. Membr. Sci. 638 (2021), 119681, 10/gmg9gf.

[12] W. Guo, H. Xia, F. Xia, X. Hou, L. Cao, L. Wang, J. Xue, G. Zhang, Y. Song, D. Zhu, Y. Wang, L. Jiang, Current rectification in temperature-responsive single nanopores, ChemPhysChem 11 (2010) 859–864, 10/c4s287.

[13] S. Howorka, Z.S. Siwy, Reading amino acids in a nanopore, Nat. Biotechnol. 38 (2020) 159–160, https://doi.org/10.1038/s41587-019-0401-y.

[14] D.M. Kanani, W.H. Fissell, S. Roy, A. Dubnisheva, A. Fleischman, A.L. Zydney, Permeability–selectivity analysis for ultrafiltration: effect of pore geometry, J. Membr. Sci. 349 (2010) 405–410, https://doi.org/10.1016/j.memsci.2009.12.003.

[15] D.M. Karl, Plastics-irradiated-etched: the Nuclepore® filter turns 45 years old, Limnol. Oceanogr. Bull. 16 (2007) 49–54, 10/gpb2hq.

[16] D. Kaya, Review—track-etched nanoporous polymer membranes as sensors: a review, J. Electrochem. Soc. 16 (2020), https://doi.org/10.1149/1945-7111/ab67a7.

[17] I. Kazeminezhad, A.C. Barnes, J.D. Holbrey, K.R. Seddon, W. Schwarzacher, Templated electrodeposition of silver nanowires in a nanoporous polycarbonate membrane from a nonaqueous ionic liquid electrolyte, Appl. Phys. A 86 (2007) 373–375, https://doi.org/10.1007/s00339-006-3783-x.

[18] K. Kececi, D. Kaya, C.R. Martin, Resistive-pulse sensing of DNA with a polymeric nanopore sensor and characterization of DNA translocation, ChemNanoMat (2021), https://doi.org/10.1002/cnma.202100424.

[19] K. Kececi, N. San, D. Kaya, Nanopore detection of double stranded DNA using a track-etched polycarbonate membrane, Talanta 144 (2015) 268–274, https://doi.org/10.1016/j.talanta.2015.06.005.

[20] T. Ma, J. Janot, S. Balme, Track-etched nanopore/membrane: from fundamental to applications, Small Methods 4 (2020), 2000366, https://doi.org/10.1002/smtd.202000366.

[21] C.R. Martin, Z.S. Siwy, Learning nature's way: biosensing with synthetic nanopores, Science 317 (2007) 331–332, https://doi.org/10.1126/science.1146126.

[22] P. Martínez-Pérez, J. García-Rupérez, Commercial polycarbonate track-etched membranes as substrates for low-cost optical sensors, Beilstein J. Nanotechnol. 10 (2019) 677–683, 10/gg7jf5.

[23] F. Maurer, A. Dangwal, D. Lysenkov, G. Müller, M.E. Toimil-Molares, C. Trautmann, J. Brötz, H. Fuess, Field emission of copper nanowires grown in polymer ion-track membranes, Nucl. Instrum. Methods Phys. Res. Sect. B Beam Interact. Mater. Atoms 245 (2006) 337–341, 10/cnqc22.

[24] G. Pérez-Mitta, A.S. Peinetti, M.L. Cortez, M.E. Toimil-Molares, C. Trautmann, O. Azzaroni, Highly sensitive biosensing with solid-state nanopores displaying enzymatically reconfigurable rectification properties, Nano Lett. 18 (2018) 3303–3310, 10/gdkctd.

[25] Y. Shen, P.O. Saboe, I.T. Sines, M. Erbakan, M. Kumar, Biomimetic membranes: a review, J. Membr. Sci. 454 (2014) 359–381, https://doi.org/10.1016/j.memsci.2013.12.019.

[26] Z. Siwy, A. Fuliński, Fabrication of a synthetic nanopore ion pump, Phys. Rev. Lett. 89 (2002), 198103, 10/c2d6qd.

[27] S. Valizadeh, J.M. George, P. Leisner, L. Hultman, Electrochemical synthesis of AgyCo multilayered nanowires in porous polycarbonate membranes, Thin Solid Films (2002) 10, https://doi.org/10.1016/s0040-6090(01)01674-1.

[28] P. Wang, M. Wang, F. Liu, S. Ding, X. Wang, G. Du, J. Liu, P. Apel, P. Kluth, C. Trautmann, Y. Wang, Ultrafast ion sieving using nanoporous polymeric membranes, Nat. Commun. 9 (2018) 569, https://doi.org/10.1038/s41467-018-02941-6.

[29] Q. Wen, D. Yan, F. Liu, M. Wang, Y. Ling, P. Wang, P. Kluth, D. Schauries, C. Trautmann, P. Apel, W. Guo, G. Xiao, J. Liu, J. Xue, Y. Wang, Highly selective ionic transport through subnanometer pores in polymer films, Adv. Funct. Mater. 26 (2016) 5796–5803, https://doi.org/10.1002/adfm.201601689.

[30] S. Wu, Y. Cheng, J. Ma, Q. Huang, Y. Dong, J. Duan, D. Mo, Y. Sun, J. Liu, H. Yao, Preparation and ion separation properties of sub-nanoporous PES membrane with high chemical resistance, J. Membr. Sci. 635 (2021), 119467, https://doi.org/10.1016/j.memsci.2021.119467.

[31] H.A. Maddah, Polypropylene as a promising plastic: a review, Am. J. Polym. Sci. (2016) 11.

[32] J. Karger-Kocsis, T. Bárány (Eds.), Polypropylene Handbook: Morphology, Blends and Composites, Springer International Publishing, Cham, 2019, https://doi.org/10.1007/978-3-030-12903-3.

[33] J. Breil, 12 - oriented film technology, in: J.R. Wagner (Ed.), Multilayer Flex. Packag, second ed., William Andrew Publishing, 2016, pp. 153–172, https://doi.org/10.1016/B978-0-323-37100-1.00012-0.

[34] J. Wagner, Multilayer Flexible Packaging: Technology and Applications for the Food, Personal Care and Over-the-counter Pharmaceutical Industries, Elsevier Science, Oxford, 2010.

[35] L.I. Kravets, S.N. Dmitriev, P.Y. Apel, The properties and porous structure of polypropylene track membranes, Radiat. Meas. 25 (1995) 729–732, https://doi.org/10.1016/1350-4487(95)00233-5.

[36] S. Heise, P. Vater, R. Brandt, K.K. Dwivedi, C. Dankmeter, On the development of polypropylene (PP) microfilters, Nucl. Tracks Radiat. Meas. 22 (1993) 909–910, https://doi.org/10.1016/0969-8078(93)90207-K.

[37] K. Awasthi, V. Kulshrestha, N.K. Acharya, M. Singh, Y.K. Vijay, Ion transport through track etched polypropylene membrane, Eur. Polym. J. 42 (2006) 883–887, https://doi.org/10.1016/j.eurpolymj.2005.09.031.

[38] P.Yu Apel, O.L. Orelovich, Etching of submicron pores in thin polypropylene films irradiated with heavy ions, Int. J. Radiat. Appl. Instrum. Part Nucl. Tracks Radiat. Meas. 19 (1991) 25–28, https://doi.org/10.1016/1359-0189(91)90138-8.

[39] P.Yu Apel, Conductometric studies of multiply charged ion track structure in various polymers, Int. J. Radiat. Appl. Instrum. Part Nucl. Tracks Radiat. Meas. 19 (1991) 29–34, 10/dtcdtw.

[40] P. Gijsman, J. Hennekens, J. Vincent, The mechanism of the low-temperature oxidation of polypropylene, Polym. Degrad. Stabil. 42 (1993) 95–105, https://doi.org/10.1016/0141-3910(93)90031-D.

[41] P. Gijsman, Polymer stabilization, in: Handb. Environ. Degrad. Mater., Elsevier, 2018, pp. 369–395, https://doi.org/10.1016/B978-0-323-52472-8.00018-6.

[42] J.C.W. Chien, H. Jabloner, Polymer reactions. IV. Thermal decomposition of polypropylene hydroperoxides, J. Polym. Sci. [A1] 6 (1968) 393–402, https://doi.org/10.1002/pol.1968.150060209.

[43] G. Zhang, C. Nam, L. Petersson, J. Jämbeck, H. Hillborg, T.C.M. Chung, Increasing polypropylene high temperature stability by blending polypropylene-bonded hindered phenol antioxidant, Macromolecules 51 (2018) 1927–1936, https://doi.org/10.1021/acs.macromol.7b02720.

[44] A. Aboulkas, K. El harfi, A. El Bouadili, Thermal degradation behaviors of polyethylene and polypropylene. Part I: pyrolysis kinetics and mechanisms, Energy Convers. Manag. 51 (2010) 1363–1369, https://doi.org/10.1016/j.enconman.2009.12.017.

[45] G. Geuskens, M.S. Kabamba, Photo-oxidation of polymers: Part IX—additional comments about a new chain scission mechanism in polyolefins, Polym. Degrad. Stabil. 5 (1983) 399–401, https://doi.org/10.1016/0141-3910(83)90044-7.

[46] I.V. Blonskaya, O.V. Kristavchuk, A.N. Nechaev, O.L. Orelovich, O.A. Polezhaeva, P.Y. Apel, Observation of latent ion tracks in semicrystalline polymers by scanning electron microscopy, J. Appl. Polym. Sci. 138 (2021), 49869, https://doi.org/10.1002/app.49869.

[47] P. Kluth, C.S. Schnohr, O.H. Pakarinen, F. Djurabekova, D.J. Sprouster, R. Giulian, M.C. Ridgway, A.P. Byrne, C. Trautmann, D.J. Cookson, K. Nordlund, M. Toulemonde, Fine structure in swift heavy ion tracks in amorphous SiO2, Phys. Rev. Lett. 101 (2008), 175503, https://doi.org/10.1103/physrevlett.101.175503.

[48] P. Kluth, C.S. Schnohr, D.J. Sprouster, A.P. Byrne, D.J. Cookson, M.C. Ridgway, Measurement of latent tracks in amorphous SiO2 using small angle X-ray scattering, Nucl. Instrum. Methods Phys. Res. Sect. B Beam Interact. Mater. Atoms 266 (2008) 2994–2997, 10/cgx2m6.

[49] X. Wang, S. Dutt, C. Notthoff, A. Kiy, P. Mota-Santiago, S.T. Mudie, M.E. Toimil-Molares, F. Liu, Y. Wang, P. Kluth, SAXS data modelling for the characterisation of ion tracks in polymers, Phys. Chem. Chem. Phys. 24 (2022) 9345–9359, https://doi.org/10.1039/D1CP05813D.

[50] P. Mota-Santiago, H. Vazquez, T. Bierschenk, F. Kremer, A. Nadzri, D. Schauries, F. Djurabekova, K. Nordlund, C. Trautmann, S. Mudie, M.C. Ridgway, P. Kluth, Nanoscale density variations induced by high energy heavy ions in amorphous silicon nitride and silicon dioxide, Nanotechnology 29 (2018), https://doi.org/10.1088/1361-6528/aaabdb.

[51] K. Möller, T. Gevert, A solid-state investigation of the desorption/evaporation of hindered phenols from low density polyethylene using FTIR and UV spectroscopy with integrating sphere: the effect of molecular size on the desorption, J. Appl. Polym. Sci. 61 (1996) 1149–1162, https://doi.org/10.1002/(SICI)1097-4628(19960815)61:7<1149::AID-APP11>3.0.CO;2-T.

[52] Z. G, N. C, M.C. Tc, Developing polypropylene bonded hindered phenol antioxidants for expanding polypropylene applications in high temperature conditions, J. Mater. Sci. Eng. 6 (2017), https://doi.org/10.4172/2169-0022.1000393.

[53] J.F. Ziegler, M.D. Ziegler, J.P. Biersack, SRIM – the stopping and range of ions in matter (2010), Nucl. Instrum. Methods Phys. Res. Sect. B Beam Interact. Mater. Atoms 268 (2010) 1818–1823, https://doi.org/10.1016/j.nimb.2010.02.091.

[54] P. Apel, A. Schulz, R. Spohr, C. Trautmann, V. Vutsadakis, Track size and track structure in polymer irradiated by heavy ions, Nucl. Instrum. Methods Phys. Res. Sect. B Beam Interact. Mater. Atoms 146 (1998) 468–474, 10/b4qr2h.

[55] M. Engel, B. Stühn, J.J. Schneider, T. Cornelius, M. Naumann, Small-angle X-ray scattering (SAXS) off parallel, cylindrical, well-defined nanopores: from random pore distribution to highly ordered samples, Appl. Phys. Mater. Sci. Process 97 (2009) 99–108, 10/fh3vqm.

[56] F. Zhang, J. Ilavsky, G.G. Long, J.P.G. Quintana, A.J. Allen, P.R. Jemian, Glassy carbon as an absolute intensity calibration standard for small-angle scattering, Metall. Mater. Trans. A 41 (2010) 1151–1158, 10/d3c9ks.

[57] P. Apel, A. Schulz, R. Spohr, C. Trautmann, V. Vutsadakis, Tracks of very heavy ions in polymers, Nucl. Instrum. Methods Phys. Res. Sect. B Beam Interact. Mater. Atoms 131 (1997) 55–63, https://doi.org/10.1016/s0168-583x(97)00389-3.

[58] D. Fink (Ed.), Fundamentals of Ion-Irradiated Polymers, Springer Berlin Heidelberg, Berlin, Heidelberg, 2004. http://link.springer.com/10.1007/978-3-66 2-07326-1. (Accessed 11 September 2020).

[59] J. Lacoste, D. Vaillant, D.J. Carlsson, Gamma-, photo-, and thermally-initiated oxidation of isotactic polypropylene, J. Polym. Sci. Part Polym. Chem. 31 (1993) 715–722, https://doi.org/10.1002/pola.1993.080310316.

[60] A. Rjeb, L. Tajounte, M.C. El Idrissi, S. Letarte, A. Adnot, D. Roy, Y. Claire, A. Périchaud, J. Kaloustian, IR spectroscopy study of polypropylene natural aging, J. Appl. Polym. Sci. 77 (2000) 1742–1748, https://doi.org/10.1002/1097-4628 (20000822)77:8<1742::AID-APP11>3.0.CO;2-T.

[61] A. Rivaton, D. Lalande, J.-L. Gardette, Influence of the structure on the γ-irradiation of polypropylene and on the post-irradiation effects, Nucl. Instrum. Methods Phys. Res. Sect. B Beam Interact. Mater. Atoms 222 (2004) 187–200, https://doi.org/10.1016/j.nimb.2004.02.012.

[62] M. Dole, The Radiation Chemistry of Macromolecules: Volume II, Elsevier, 2013.

[63] M. Iring, F. Tüdős, Thermal oxidation of polyethylene and polypropylene: effects of chemical structure and reaction conditions on the oxidation process, Prog. Polym. Sci. 15 (1990) 217–262, https://doi.org/10.1016/0079-6700(90)90029-Z.

[64] D. Fink, Transport Processes in Ion-Irradiated Polymers, Springer Berlin Heidelberg, Berlin, Heidelberg, 2004. http://link.springer.com/10.1007/978-3-66 2-10608-2. (Accessed 11 September 2020).

[65] P.Yu Apel, A.Yu Didyk, A.G. Salina, Physico-chemical modification of polyolefins irradiated by swift heavy ions, Nucl. Instrum. Methods Phys. Res. Sect. B Beam Interact. Mater. Atoms 107 (1996) 276–280, https://doi.org/10.1016/0168-583X (95)01038-6.